# Structure and UV–Vis spectroscopy of nitrosylthiolatoferrate mononuclear complexes

Maria Jaworska [a,*], Zofia Stasicka [b]

[a] *Department of Theoretical Chemistry, University of Silesia, Szkolna 9, 40-006 Katowice, Poland*
[b] *Faculty of Chemistry, Jagiellonian University, Ingardena 3, 30-060 Kraków, Poland*

## Abstract

Density functional calculations for the $[(RS)_xFe(NO)_{4-x}]^-$ ($R = CH_3$) compounds are carried out using the DFT method with the B3LYP functional. The results can be verified by the experimental data only in the case of the $[(RS)_2Fe(NO)_2]^-$ complex. The experimentally characterised molecular structure of $[(RS)_2Fe(NO)_2]^-$ (where $(RS)_2 = (SCH_2CH_2NMeCH_2CH_2CH_2NMeCH_2CH_2S)$) is properly reproduced by the RB3LYP method. The discrepancy between the calculated spin densities with the integral spin observed experimentally is interpreted in terms of antiferromagnetic coupling between the Fe(III) centre and the $NO^-$ ligands. The theoretical analysis gives a good account of some properties observed in these compounds. In particular, the electronic spectrum calculated by the TDDFT method for $[(CH_3S)_2Fe(NO)_2]^-$ is similar in shape to the experimental one, although is hypsochromically shifted. The LLCT ($S_\pi \to \pi_{NO}^*$), LMCT ($S_\pi \to d$) or ($\pi_{NO}^* \to d + S_\pi \to d$) and MLCT ($d \to \pi_{NO}^*$) transitions are mostly responsible for absorption of the $[(RS)_xFe(NO)_{4-x}]^-$ complexes within UV–Vis. The chemical reactivity of $[(RS)_2Fe(NO)_2]^-$ is interpreted basing on the calculated effect of a polar solvent on the ligand polarity and on the character of the HOMO and LUMO orbitals.
© 2004 Elsevier B.V. All rights reserved.

*Keywords:* Nitrosylthiolatoferrate mononuclear complexes; Electronic structure; Electronic spectra; DFT; TDDFT

## 1. Introduction

Although many iron complexes with nitrosyl and sulfur ligands had been studied for more than 100 years, their contribution to the biomedical processes was revealed only in the 1980s. Now a number of nitrosylthiolatoferrates are known both as mononuclear complexes and clusters containing two, three, four and six iron centres, they are recognized or considered, to play a role of the NO-donor in biomedical systems [1,2]. This behaviour is of relevance to vital functions of living organisms where fast NO-bonding, NO-carrying and NO-release processes are required.

The aim of this study was to use the DFT method to analyse a correlation between the structure and bonding character in the nitrosylthiolatoferrates and their reactivities. We also calculated the electronic spectra of the compounds under investigation with the TDDFT method. An understanding of the bonding in NO-donors was the special aim of these calculations. As these compounds occur in a variety of geometrical forms, containing different numbers of centres and the varied Fe:NO:RS ratios, a number of factors can influence their ability to behave as the NO-carriers. To make a systematic study of the effects, we decided to analyse first the relationship in the mononuclear Fe-species. This paper summarises the results of the DFT calculations concerning tetrahedral $[(RS)_xFe(NO)_{4-x}]^-$ complexes, where $x = 2$ or 3. The first of them belongs to a family of dinitrosyl iron thiol complexes (DNICs), which are known to be responsible for storage and transport of NO in the biological tissues [2].

The complexes investigated in this work have the $\{Fe(NO)_2\}^9$ and $\{Fe(NO)\}^7$ cores for $x = 2$ and 3, respectively, according to the Enemark and Feltham notation [3]. The qualitative description of the geometry dependence of metal–NO fragment on the electronic

---
* Corresponding author. Tel.: +48-12-633-5392; fax: +48-12-633-53-92.
*E-mail addresses:* mj@tc3.ich.us.edu.pl (M. Jaworska), stasicka@chemia.uj.edu.pl (Z. Stasicka).

configuration of $\{M(NO)\}^n$ group was given by Enemark and Feltham and others [3–5]. Six-coordinated nitrosyl-iron complexes with the $\{Fe(NO)\}^7$ core possess an $S = 3/2$ or $1/2$ ground state. It has been shown by X-ray absorption, resonance Raman, MCD, EPR, Mössbauer spectroscopy and DFT calculations that the $\{Fe(NO)\}^7$ $(S = 3/2)$ species are high spin ferric $(S = 5/2)$ antiferromagnetically coupled to $NO^-$ $(S = 1)$ [6–9]. One of the aims of the present study is to elucidate the mode of the NO-bonding in the four-coordinated nitrosylthiolate complexes of iron.

## 2. Calculational procedures

GAUSSIAN98 program [10] was used in the calculations. The calculations were performed using the DFT method with the B3LYP functional [11,12]. The electronic spectra were calculated by the TDDFT method [13]. The basis set used comprised the LANL2DZ basis [14] on Fe and S with an additional d function on iron ($\alpha = 0.1214$) and on sulfur ($\alpha = 0.7$), DZV(P) basis on N, C and O and DZV on H [15]. To include the solvent influence, the PCM model [16,17] was used with water as the solvent. Calculations were done with the RB3LYP and UB3LYP methods. For the UB3LYP wave functions, the stability tests were performed with the STABLE(RUHF) option in the GAUSSIAN98 program. Additional tests with the READ(ALTER) option were done, where the $\alpha$ and $\beta$ HOMO and LUMO orbitals were interchanged. In all cases, no function with a lower energy was found. The electronic spectra were calculated with the UB3LYP method, which is the one accessible in GAUSSIAN98 for the open shell wave functions.

## 3. Geometry and electronic structure of the $[(RS)_x Fe(NO)_{4-x}]^-$ complexes

The calculations of electronic structure and spectra of $[(RS)_2Fe(NO)_2]^-$ (**I**) and $[(RS)_3Fe(NO)]^-$ (**II**) with a methyl group as R were performed. These species are formed in reactions of iron salts with nitric oxide and thiols [2,18–20].

### 3.1. $[(CH_3S)_2Fe(NO)_2]^-$ (**I**)

The geometry of **I** was optimized with the RB3LYP method. Two conformations found for **I**, denoted **IA** and **IB**, are shown in Fig. 1. The geometry of **IA** was also optimized with the UB3LYP method. As the experimental spin of $[(RS)_2Fe(NO)_2]^-$ amounts to $1/2$ [1,18–20], the calculations were performed with $S = 1/2$. To test, however, if the B3LYP method gives the correct spin state for **I**, the calculations with $S = 3/2$ for **IA** were also done at the RB3LYP level. The energies
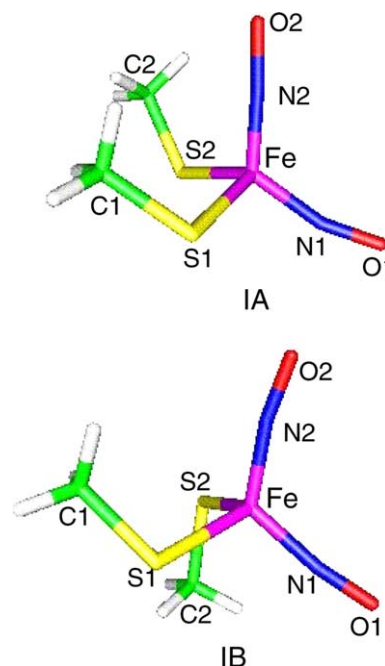


Fig. 1. Conformations of $[(CH_3S)_2Fe(NO)_2]^-$.

obtained using the different methods with and without the solvent influence are presented in Table 1. As expected, the energy of **IA** in the quartet state is higher than that of the doublet state, in accordance with the experiment [1,18–20]. The energy differences between the two conformers are very small.

The geometric parameters of **IA** and **IB** are collected in Table 2, together with the experimental geometry of the $[Fe(SCH_2CH_2NMeCH_2CH_2CH_2NMeCH_2CH_2S)H(NO)_2]$ complex [21], which structurally and electronically is closely related to **I**. The comparison of the calculated parameters with the experimental ones reveals that RB3LYP gives better agreement with the experiment than UB3LYP. The RB3LYP optimized Fe–NO distances are in the range 1.629–1.642 Å, a little shorter than in the experimental values. The Fe–S distances vary from 2.308 to 2.315 Å and are a little longer than

Table 1
Energy of **I** for the RB3LYP optimized geometry (W – water influence included)

| Method | $S$ | $E$ (a.u.) | $\langle S^2 \rangle$ | $\Delta E^a$ (kJ) |
|--------|-----|-----------|----------------------|-------------------|
| **IA** | | | | |
| RB3LYP | 3/2 | −483.527542 | 3.75 | |
| RB3LYP | 1/2 | −483.538948 | 0.75 | 0.0 |
| UB3LYP | 1/2 | −483.554790 | 2.020 | 0.0 |
| UB3LYP-W | 1/2 | −483.617265 | 1.849 | 0.0 |
| **IB** | | | | |
| RB3LYP | 1/2 | −483.541550 | 0.75 | −11.0 |
| UB3LYP | 1/2 | −483.557898 | 1.887 | −8.1 |
| UB3LYP-W | 1/2 | −483.618024 | 1.837 | 2.0 |

$^a$ Relatively to **IA**.

Table 2
RB3LYP (UB3LYP in parentheses) optimized geometric parameters of **I**

| **IA** | | | | | |
|---|---|---|---|---|---|
| Fe–N1 | 1.642(1.780) | Fe–N1—O1 | 162.6(164.6) | N1—Fe—S1–C1 | −176.8(−172.5) |
| Fe–N2 | 1.629(1.753) | Fe–N2–O2 | 176.3(154.3) | N1–Fe–S2–C2 | −146.6(−144.4) |
| Fe–S[a] | 2.314(2.361) | N1–Fe–N2 | 123.5(119.1) | N2–Fe–S1–C1 | 51.5(60.6) |
| S1–C1[a] | 1.837(1.840) | S1–Fe–S2 | 109.0(110.4) | N2—Fe–S2–C2 | −12.8(−14.2) |
| O–N[a] | 1.193(1.200) | | | | |
| **IB** | | | | | |
| Fe–N1 | 1.635 | Fe–N1–O1 | 169.4 | N1–Fe–S1–C1 | 178.5 |
| Fe–N2 | 1.634 | Fe–N2–O2 | 170.6 | N1–Fe–S2–C2 | 47.8 |
| Fe–S[a] | 2.308 | N1–Fe–N2 | 120.5 | N2–Fe–S1–C1 | 47.5 |
| S–C[a] | 1.837 | S1–Fe–S2 | 105.5 | N2–Fe–S2–C2 | 178.8 |
| O–N[a] | 1.193 | | | | |
| Experimental[b] | | | | | |
| Fe–N1 | 1.64 | Fe–N1–O1 | 169.1 | | |
| Fe–N2 | 1.67 | Fe–N2–O2 | 170.5 | | |
| Fe–S[a] | 2.273 | N1–Fe–N2 | 118.3 | | |
| S–C[a] | 1.82 | S1–Fe–S2 | 109.2 | | |
| O–N[a] | 1.165 | | | | |

Bond lengths in Å, angles in degrees (°).
[a] Average value.
[b] Ref. [21].

the experimental ones. In general, the bond distances agree up to 0.03–0.04 Å with the experimental ones. The Fe–N–O angles from the RB3LYP optimization of **IB** agree very well with the experimental ones. As in the experimental geometry [21], the tetrahedral geometry is strongly distorted with the largest angle at the iron atom, 119.1–123.5, which is subtended by two nitrosyl ligands. The UB3LYP optimized bond lengths for **IA** are much too long, especially for the Fe–NO bonds, which differ by about 0.1 Å from the experimental ones. Because of that, the results presented further are obtained with the use of the RB3LYP optimized geometry.

Fig. 2 shows the α (spin-up) and β (spin-down) orbitals from the UB3LYP calculations. The bonding $\pi^*_{Fe–NO}$ orbitals of α and β spin are localised on different parts of the molecule – α orbitals (H31–H35) are mainly d in character, β orbitals (H31–H36) have prevalent NO character. In both cases they are mixed with sulfur orbitals. The highest occupied orbitals (H36–H39 for α spin and H37–H38 for β spin) are sulfur π orbitals. The α LUMO orbitals (L40–L43) are antibonding $\pi^*_{Fe–NO}$ orbitals, they are localised mainly on the nitrosyl groups, while the antibonding β orbitals (L39–L43) are localised on the iron d orbitals. Starting from L44 the 4p orbitals of iron do appear. It can be seen in Table 1 that the expectation value of $\hat{S}^2$ operator is significantly different from 0.75 for the UB3LYP wave functions. The localisation of α and β orbitals is not complete – the $\pi^*_{NO}$ orbitals have tails on the d orbitals and vice versa.

The molecular orbital energy diagrams calculated with and without the water effect are shown in Fig. 3 for the conformation **IA**. These diagrams illustrate that in all cases the HOMO orbitals are composed mostly of the sulfur orbitals, whereas the LUMOs are localised on the NO ligands and the central ion. Moreover, the diagrams reveal that the energy levels of the two sets of the sulfur centred orbitals are significantly separated – the $S_\pi$ orbitals are much higher in energy than $S_\sigma$. The former mix with the high lying occupied β orbitals of the $\pi^*_{NO}$ type, whereas the latter – with the low-lying occupied α d-type orbitals. The α and β unoccupied orbitals of $\pi^*_{NO}$ and d type, respectively, are of similar energy. Molecular orbital energies are strongly sensitive to the solvent effect. The relative orbital spacing does not change considerably, but in the solvent all orbital levels are shifted down by about 4 eV.

In Table 3, the atomic charges and spin densities are collected for **IA** and **IB** from the UB3LYP calculations. The charges on the iron atom without water are positive of rather moderate value (0.122 for **IA** and 0.101 for **IB**). In the calculations with solvent, the iron charges are lowered to very small positive values (0.020 for **IA**) or slightly negative (−0.004 for **IB**). The charges on the sulfur atoms are negative. The total charges of the NO groups are also negative. It is noteworthy that the negative charge is mostly localised on the oxygen atom. The presence of a solvent has rather small effect on the values of spin densities. There is a large positive spin density on the iron atom of about 2.5 and negative spin densities of about −0.5 on the nitrogen and oxygen atoms. There are also positive spin densities of about 0.2 on the sulfur atoms. The overall picture emerging from the unrestricted molecular orbital form and the charge and spin density distribution can be described as the $Fe^{3+}$ ion ($S = 5/2$) antiferromagnetically coupled to the two $NO^-$ ions each with $S = 1$, which gives the total spin of the molecule
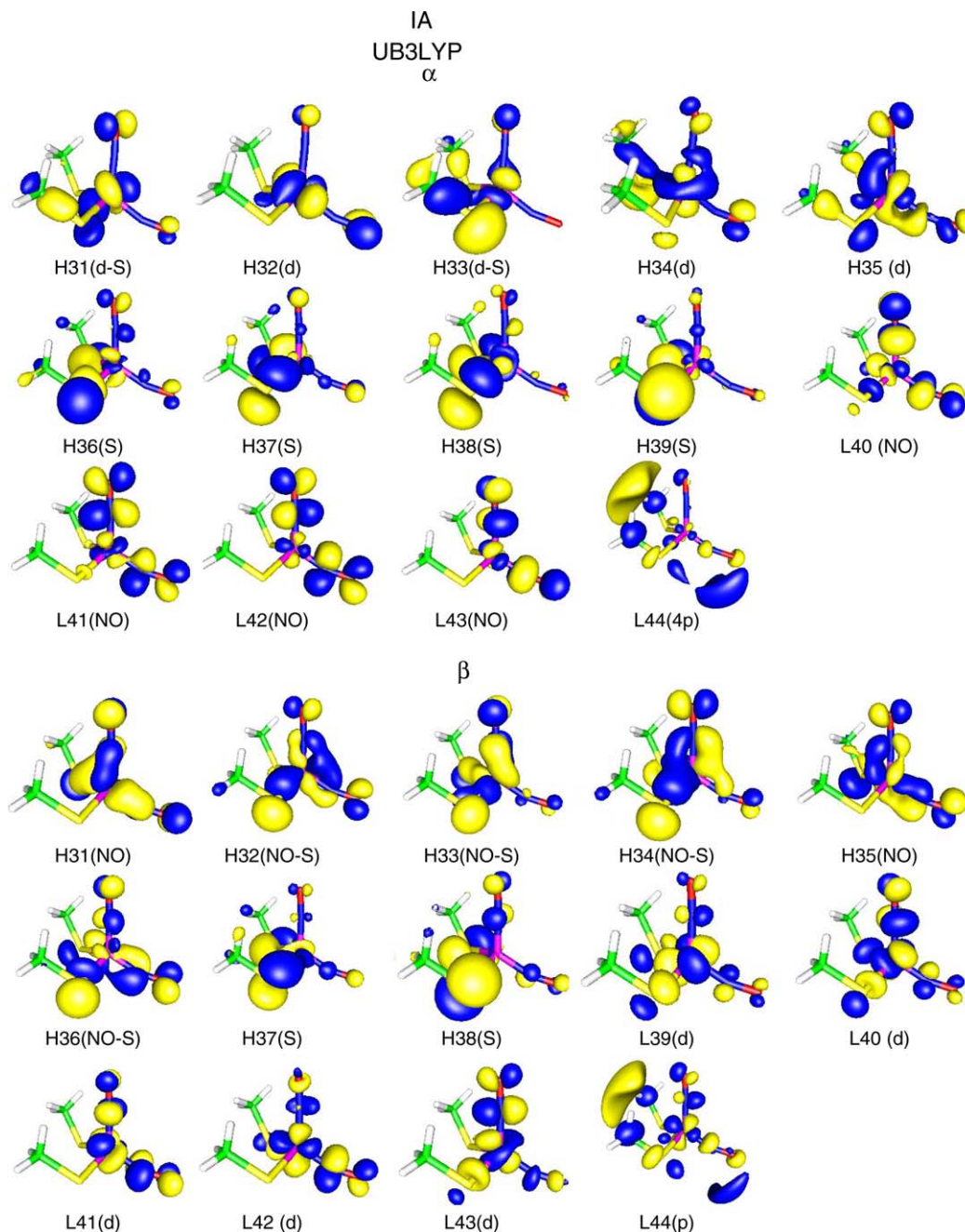
IA
UB3LYP
α



H31(d-S)    H32(d)    H33(d-S)    H34(d)    H35 (d)

H36(S)    H37(S)    H38(S)    H39(S)    L40 (NO)

L41(NO)    L42(NO)    L43(NO)    L44(4p)

β

H31(NO)    H32(NO-S)    H33(NO-S)    H34(NO-S)    H35(NO)

H36(NO-S)    H37(S)    H38(S)    L39(d)    L40 (d)

L41(d)    L42 (d)    L43(d)    L44(p)

Fig. 2. UB3LYP α and β molecular orbitals of **IA**.

equal to 1/2. The atomic spin densities on the iron atom and NO groups are much smaller than the absolute values 5.0 and 2.0, respectively. This results from the fact that the localisation of α and β orbitals is not complete, which allows for their effective overlap and the antiferromagnetic coupling. In the case of a complete localisation, higher spin states would be favoured.

The iron charge is also far from the formal 3+ charge, which can be explained by a strong charge donation from both the $SR^-$ ions and the $NO^-$ ions. This is also reflected in the charges of all these ligands, which are much smaller than 1−. The description of the iron centre as Fe(III) is

also inconsistent with the chemical behaviour of the **I** complex, which is rather characteristic of a species with the Fe(−I) centre (vide infra). The calculations show for a similar mode of bonding for the NO ligand to the iron atom as in some octahedral complexes [6–9].
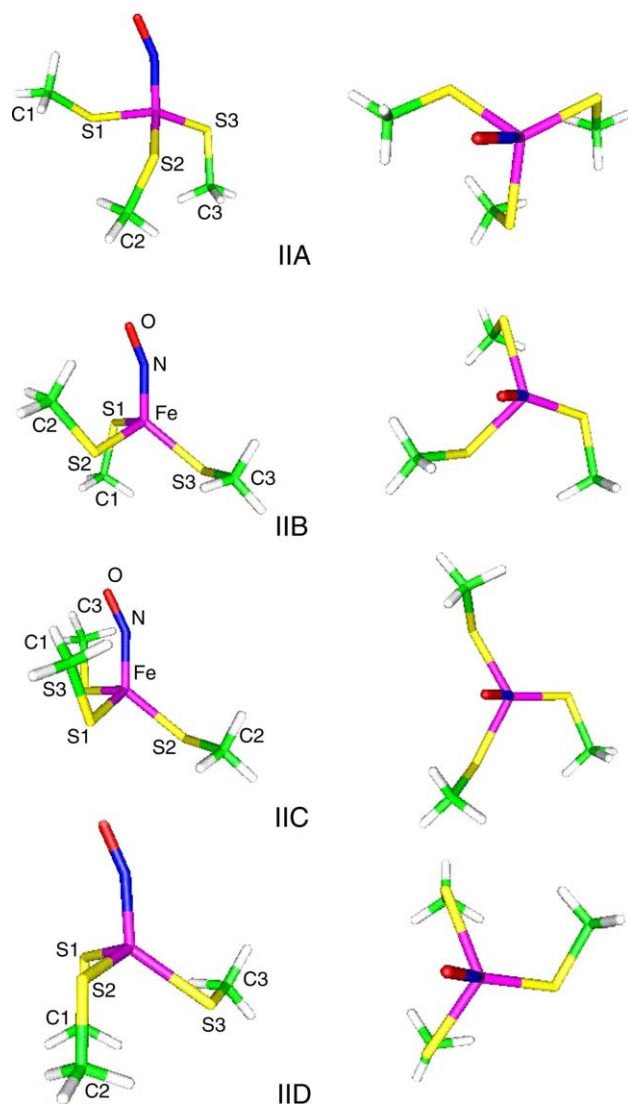
### 3.2. $[(CH_3S)_3Fe(NO)]^-$ (**II**)

The RB3LYP calculations for **II** were carried out for spin quantum number 1/2 and 3/2 with the geometry optimization. The UB3LYP calculations were performed with the RB3LYP optimized geometry. For
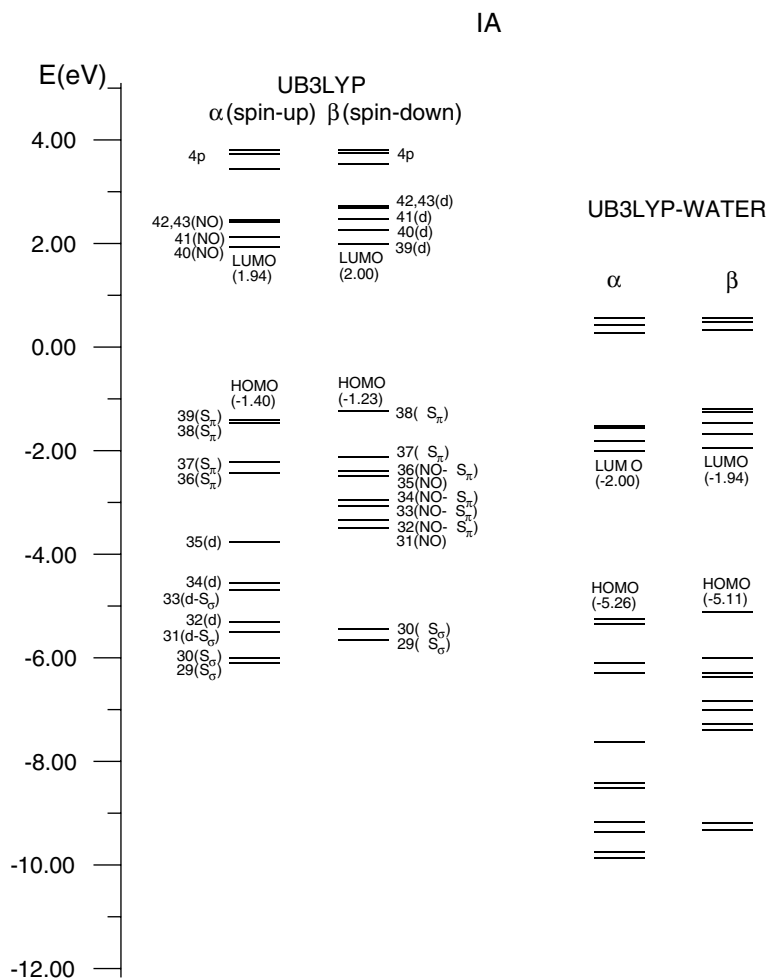
Fig. 3. Orbital energy diagrams for **IA**. Energy of HOMO and LUMO orbitals is shown in parentheses.

Table 3
UB3LYP atomic charges and spin densities of **I** (W – water)

| Method[a] | S | Fe | S1 | S2 | C1 | C2 | N1 | O1 | N2 | O2 |
|---|---|---|---|---|---|---|---|---|---|---|
| *Charges* | | | | | | | | | | |
| **IA** | | | | | | | | | | |
| UB3LYP | 1/2 | 0.122 | −0.170 | −0.169 | −0.082 | −0.103 | −0.109 | −0.199 | −0.083 | −0.204 |
| UB3LYP-W | 1/2 | 0.020 | −0.179 | −0.186 | −0.028 | −0.034 | −0.103 | −0.191 | −0.099 | −0.197 |
| | | | | | | | | | | |
| **IB** | | | | | | | | | | |
| UB3LYP | 1/2 | 0.101 | −0.176 | −0.176 | −0.077 | −0.077 | −0.096 | −0.201 | −0.094 | −0.200 |
| UB3LYP-W | 1/2 | −0.004 | −0.166 | −0.198 | −0.030 | 0.000 | −0.093 | −0.185 | −0.124 | −0.196 |
| | | | | | | | | | | |
| *Spin densities* | | | | | | | | | | |
| **IA** | | | | | | | | | | |
| UB3LYP | 1/2 | 2.513 | 0.195 | 0.200 | −0.007 | −0.005 | −0.532 | −0.442 | −0.510 | −0.670 |
| UB3LYP-W | 1/2 | 2.374 | 0.190 | 0.195 | −0.007 | −0.005 | −0.496 | −0.424 | −0.451 | −0.394 |
| | | | | | | | | | | |
| **IB** | | | | | | | | | | |
| UB3LYP | 1/2 | 2.425 | 0.194 | 0.194 | −0.007 | −0.007 | −0.497 | −0.413 | −0.493 | −0.411 |
| UB3LYP-W | 1/2 | 2.348 | 0.213 | 0.205 | −0.008 | −0.008 | −0.466 | −0.408 | −0.481 | −0.414 |

[a] RB3LYP geometry.

Fig. 4. Conformations of **II**.

Table 4
Energy of **II** (W – water)

| Method[a] | S | $E^a$ (a.u.) | $\langle S^2 \rangle$ | $\Delta E^b$ (kJ) |
|---|---|---|---|---|
| **IIA** | | | | |
| RB3LYP | 1/2 | −403.632038 | 0.75 | 0.0 |
| UB3LYP | 1/2 | −403.640223 | 1.367 | 0.0 |
| RB3LYP | 3/2 | −403.641202 | 3.75 | 0.0 |
| UB3LYP | 3/2 | −403.660323 | 4.433 | 0.0 |
| UB3LYP-W | 3/2 | −403.720728 | 4.437 | 0.0 |
| **IIB** | | | | |
| RB3LYP | 1/2 | −403.629659 | 0.75 | 6.2 |
| UB3LYP | 1/2 | −403.637955 | 1.348 | 5.9 |
| RB3LYP | 3/2 | −403.642540 | 3.75 | −3.5 |
| UB3LYP | 3/2 | −403.659945 | 4.406 | 1.0 |
| UB3LYP-W | 3/2 | −403.720226 | 4.411 | 1.3 |
| **IIC** | | | | |
| RB3LYP | 1/2 | −403.630138 | 0.75 | 5.0 |
| UB3LYP | 1/2 | −403.638833 | 1.316 | 3.6 |
| RB3LYP | 3/2 | −403.639310 | 3.75 | 5.0 |
| UB3LYP | 3/2 | −403.655219 | 4.386 | 13.4 |
| UB3LYP-W | 3/2 | −403.718239 | 4.337 | 6.5 |
| **IID** | | | | |
| RB3LYP | 1/2 | −403.630936 | 0.75 | 3.0 |
| UB3LYP | 1/2 | −403.638702 | 1.387 | 4.0 |
| RB3LYP | 3/2 | −403.642380 | 3.75 | −3.0 |
| UB3LYP | 3/2 | −403.659650 | 4.403 | 1.8 |
| UB3LYP-W | 3/2 | −403.720364 | 4.378 | 0.9 |

[a] RB3LYP geometry.
[b] Relatively to **IIA**.

Table 5
The geometric parameters of **IIA–IID** (RB3LYP, quartet state)

| | **IIA** | **IIB** | **IIC** | **IID** |
|---|---|---|---|---|
| Fe–N | 1.682 | 1.682 | 1.686 | 1.686 |
| N–O | 1.186 | 1.189 | 1.192 | 1.185 |
| Fe–S[a] | 2.322 | 2.314 | 2.320 | 2.322 |
| S1–C[a] | 1.841 | 1.840 | 1.839 | 1.841 |
| Fe–N–O | 157.7 | 157.9 | 154.4 | 159.6 |
| N–Fe–S1 | 101.6 | 103.2 | 99.9 | 98.2 |
| N–Fe–S2 | 103.8 | 107.0 | 129.8 | 100.3 |
| N–Fe–S3 | 117.0 | 128.8 | 100.5 | 128.8 |
| S1–Fe–S2 | 109.4 | 114.7 | 104.6 | 120.0 |
| S1–Fe–S3 | 108.6 | 106.4 | 119.6 | 106.5 |
| S2–Fe–S3 | 115.2 | 103.5 | 103.8 | 104.4 |
| N–Fe–S1–C1 | −45.6 | −164.4 | 3.6 | −173.7 |
| N–Fe–S2–C2 | 154.0 | 26.2 | 72.6 | 175.0 |
| N–Fe–S3–C3 | 160.3 | 62.2 | 14.6 | −71.5 |

[a] Average values.

$S = 1/2$ the UB3LYP calculations were done without water, for $S = 3/2$ the calculations were performed with and without water. Four conformations of **II** (**IIA–IID**) were found, they are presented in Fig. 4. The respective energies of **II** are gathered in Table 4. The energy of the quartet state is lower than the energy of the doublet state for both RB3LYP and UB3LYP in all cases. For the quartet state, unrestricted wave function **IIC** conformer has the highest energy and **IIA** has the lowest. The largest energy difference between **IIA** and the remaining conformations is equal to 13 kJ; it goes down about two times in water. The $\langle S^2 \rangle$ value of UB3LYP wave functions is notably different from 3.75 (about 4.4), which again indicates the localization of the α and β molecular orbitals on the different parts of the molecule.

The RB3LYP optimized geometry parameters are collected in Table 5 for the conformations **IIA–IID**. The Fe–NO bond length is slightly longer (1.682–1.686 Å), whereas the Fe–N–O angle is somewhat smaller (154.4°–159.6°) than in **I**. This may be interpreted in a weaker π-bonding between Fe and the NO group.

In Fig. 5, the UB3LYP α and β molecular orbitals of **IIA** are depicted. Similarly as in **I**, α and β orbitals are localised on different parts of the molecule. The six highest occupied α molecular orbitals (H35–H40) are the $S_\pi$ type orbitals. The lower lying orbitals (H29–H34) are

mainly the iron d orbitals; some of them are mixed with the $S_\sigma$ orbitals. The two lowest $\alpha$ unoccupied orbitals are of the $\pi^*_{NO}$ character. They are followed by the 4p orbitals of the iron atom. The three HOMO orbitals of the $\beta$ set are of the $S_\pi$ type. The lower energy ones are of the $\pi^*_{NO}$ character and they mix with the $S_\sigma$ orbitals. The five LUMO orbitals (L39–L42) are of metal d-type followed by 4p orbitals.
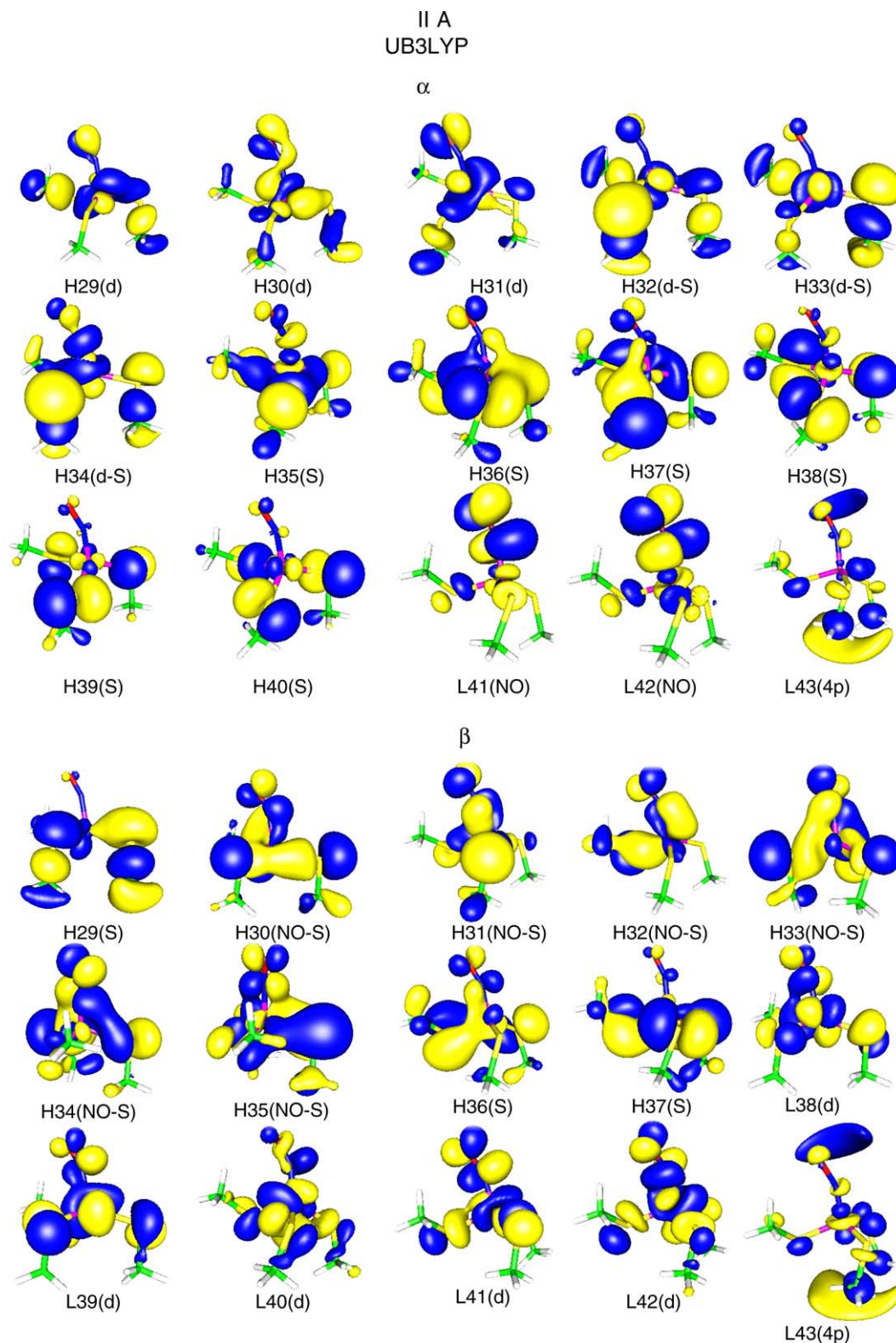


Fig. 5. UB3LYP $\alpha$ and $\beta$ molecular orbitals of **IIA**.

Table 6
UB3LYP atomic charges and spin densities of **II** (W – water)

| Method | Spin | Fe | S1 | S2 | S3 | C1 | C2 | C3 | N | O |
|---|---|---|---|---|---|---|---|---|---|---|
| *Charges* | | | | | | | | | | |
| **IIA** | | | | | | | | | | |
| UB3LYP | 3/2 | −0.007 | −0.150 | −0.175 | −0.199 | −0.074 | −0.070 | −0.072 | −0.090 | −0.159 |
| UB3LYP-W | 3/2 | −0.163 | −0.136 | −0.183 | −0.229 | −0.005 | 0.012 | 0.003 | −0.169 | −0.127 |
| | | | | | | | | | | |
| **IIB** | | | | | | | | | | |
| UB3LYP | 3/2 | 0.007 | −0.138 | −0.172 | −0.136 | −0.096 | −0.079 | −0.092 | −0.117 | −0.173 |
| UB3LYP-W | 3/2 | −0.150 | −0.180 | −0.132 | −0.201 | 0.026 | −0.021 | −0.015 | −0.187 | −0.137 |
| | | | | | | | | | | |
| **IIC** | | | | | | | | | | |
| UB3LYP | 3/2 | −0.013 | −0.169 | −0.149 | −0.184 | −0.043 | −0.085 | −0.078 | −0.108 | −0.167 |
| UB3LYP-W | 3/2 | −0.189 | −0.115 | −0.175 | −0.152 | −0.030 | −0.018 | −0.021 | −0.156 | −0.139 |
| | | | | | | | | | | |
| **IID** | | | | | | | | | | |
| UB3LYP | 3/2 | −0.013 | −0.164 | −0.167 | −0.186 | −0.068 | −0.062 | −0.083 | −0.100 | −0.154 |
| UB3LYP-W | 3/2 | −0.181 | −0.155 | −0.163 | −0.210 | −0.004 | −0.008 | −0.021 | −0.130 | −0.131 |
| | | | | | | | | | | |
| *Spin densities* | | | | | | | | | | |
| **IIA** | | | | | | | | | | |
| UB3LYP | 3/2 | 3.199 | 0.226 | 0.246 | 0.254 | −0.004 | −0.008 | −0.006 | −0.503 | −0.443 |
| UB3LYP-W | 3/2 | 3.134 | 0.256 | 0.272 | 0.267 | −0.004 | −0.009 | −0.007 | −0.476 | −0.474 |
| | | | | | | | | | | |
| **IIB** | | | | | | | | | | |
| UB3LYP | 3/2 | 3.154 | 0.228 | 0.234 | 0.249 | −0.005 | −0.002 | −0.005 | −0.474 | −0.415 |
| UB3LYP-W | 3/2 | 3.113 | 0.285 | 0.258 | 0.248 | −0.013 | −0.006 | −0.003 | −0.464 | −0.456 |
| | | | | | | | | | | |
| **IIC** | | | | | | | | | | |
| UB3LYP | 3/2 | 3.168 | 0.275 | 0.225 | 0.233 | 0.012 | 0.005 | 0.002 | −0.488 | −0.428 |
| UB3LYP-W | 3/2 | 3.062 | 0.256 | 0.235 | 0.257 | −0.006 | −0.002 | −0.006 | −0.413 | −0.419 |
| | | | | | | | | | | |
| **IID** | | | | | | | | | | |
| UB3LYP | 3/2 | 3.199 | 0.239 | 0.262 | 0.207 | −0.009 | −0.011 | −0.001 | −0.487 | −0.432 |
| UB3LYP-W | 3/2 | 3.123 | 0.263 | 0.281 | 0.213 | −0.010 | −0.011 | −0.001 | −0.451 | −0.442 |

In Table 6, the atomic charges and spin densities of **IIA**–**IIC** for the quartet state are presented. The charge on the iron atom is negative with and without water for all the four conformations except for **IIB**. The more negative Fe charge in **II** than in **I** may be explained by stronger charge donation coming from the three $SCH_3^-$ ligands in the case of **II** than from two such groups in **I**, as well as by the weaker $\pi$-bonding with the NO ligand. The charge on the NO group is negative, as in **I**. It can be noted that the NO charges are somewhat smaller than in **I**.

The electronic structure of **II** may be described as the $Fe^{3+}$ cation of spin 5/2 antiferromagnetically coupled to the $NO^-$ anion with $S = 1$, yielding the total spin 3/2. The EPR experimental data are ambiguous [20], but not contradictory to the total spin resulting from the DFT calculations.

## 4. Electronic spectra

### 4.1. **I**

The UV/VIS experimental spectrum of **I** can be measured only in the presence of a large excess of thiolate, otherwise the monomer readily undergoes a reversible conversion to the di-nucleated form, [Fe$_2$($\mu$-SR)$_2$(NO)$_4$]. Such a solution exhibits the paramagnetic properties of **I**, whereas its spectrum is dominated by the much stronger absorption due to the dimer [18,19,22–24]. This behaviour resulted in some wrong assignments [2,18], but correct electronic spectrum of **I** ($RS^-$ = cysteamine chloride) consists of a strong band at 392 nm and two moderate bands at 603 and 772 nm [19]. There is also a steep increase in the absorption below 300 nm [19] in the spectrum of **I**.

Table 7 presents the calculated transition energies, wavelengths, oscillator strengths and the most important excitations for **IA** calculated with the water effect. Only the calculated spectrum of **IA** is described, since the spectra of both conformers are very similar. As mentioned previously the spectra are determined in the UB3LYP formalism, the only one possible for the open-shell system in the GAUSSIAN program. The calculations result in many transitions with very small oscillator strengths. Only the transitions with the oscillator strengths larger than 0.0050 are presented, except for the lowest energy transitions, which are shown also in the case of smaller oscillator strengths. In Fig. 6, the total spectra of **IA** and **IB** in water are drawn with the
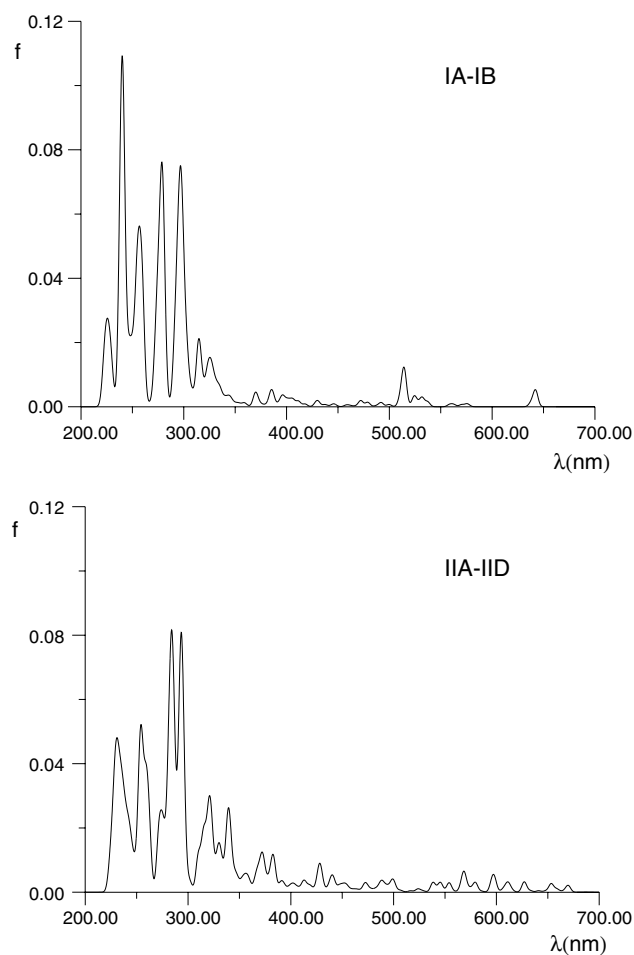
Table 7
Calculated transition energies, wavelengths, oscillator strengths and the most important excitations for **IA** (water)

| | |
|---|---|
| 1.93 eV, 642.3 nm, $f = 0.0040$ | 38(S)α → 40(NO)α |
| | 38(S)β → 39(d)β |
| 2.15 eV, 575.5 nm, $f = 0.0017$ | 38(S)α → 40(NO)α |
| | 35(NO)β → 39(d)β |
| 2.30 eV, 537.2 nm, $f = 0.0030$ | 38(S)α → 40(NO)α |
| | 39(S)α → 40(NO)α |
| | 38(S)β → 40(d)β |
| 2.36 eV, 524.7 nm, $f = 0.0037$ | 39(S)α → 40(NO)α |
| | 38(S)β → 40(d)β |
| | 38(S)β → 43(d)β |
| 2.36 eV, 523.9 nm, $f = 0.0030$ | 38(S)α → 41(NO)α |
| | 39(S)α → 41(NO)α |
| | 35(NO)β → 41(d)β |
| 2.41 eV, 513.8 nm, $f = 0.0107$ | 39(S)α → 41(NO)α |
| | 39(S)α → 43(NO)α |
| 2.62 eV, 472.2 nm, $f = 0.0038$ | 35(NO)β → 41(d)β |
| | 38(S)β → 41(d)β |
| 3.05 eV, 405.9 nm, $f = 0.0040$ | 36(NO–S)β → 39(d)β |
| | 37(S)β → 40(d)β |
| 3.69 eV, 335.2 nm, $f = 0.0078$ | 36(S)α → 43(NO)α |
| | 33(NO–S)β → 41(d)β |
| 3.75 eV, 330.6 nm, $f = 0.0068$ | 36(S)α → 43(NO)α |
| | 33(NO–S)β → 41(d)β |
| | 34(NO–S)β → 41(d)β |
| 3.79 eV, 326.4 nm, $f = 0.0074$ | 33(NO–S)β → 43(d)β |
| | 36(NO–S)β → 42(d)β |
| 3.89 eV, 318.5 nm, $f = 0.0079$ | 32(NO–S)β → 42(d)β |
| | 34(NO–S)β → 42(d)β |
| 4.08 eV, 303.3 nm, $f = 0.0127$ | 35(d)α → 40(NO)α |
| | 31(NO)β → 40(d)β |
| | 34(NO–S)β → 40(d)β |
| | 34(NO–S)β → 41(d)β |
| 4.10 eV, 301.8 nm, $f = 0.0169$ | 31(NO)β → 43(d)β |
| | 32(NO–S)β → 40(d)β |
| | 32(NO–S)β → 41(d)β |
| 4.16 eV, 297.6 nm, $f = 0.0581$ | 35(d)α → 40(NO)α |
| | 34(NO–S)β → 40(d)β |
| 4.18 eV, 296.4 nm, $f = 0.0344$ | 31(NO)β → 41(d)β |
| | 33(NO–S)β → 43(d)β |
| | 36(NO–S)β → 41(d)β |
| 4.24 eV, 291.9 nm, $f = 0.0121$ | 31(NO)β → 41(d)β |
| | 32(NO–S)β → 42(d)β |
| | 34(NO–S)β → 41(d)β |
| 4.25 eV, 291.0 nm, $f = 0.0189$ | 31(NO)β → 40(d)β |
| | 31(NO)β → 42(d)β |
| | 31(NO)β → 43(d)β |
| 4.41 eV, 280.7 nm, $f = 0.0324$ | 35(d)α → 42(NO)α |
| | 34(NO–S)β → 42(d)β |
| | 34(NO–S)β → 43(d)β |
| 4.51 eV, 274.4 nm, $f = 0.0441$ | 35(d)α → 42(NO)α |
| | 31(NO–S)β → 43(d)β |
| | 34(NO–S)β → 43(d)β |

Table 7 (*continued*)

| | |
|---|---|
| 4.77 eV, 259.9 nm, $f = 0.0252$ | 39(S)α → 44(4p)α |
| | 38(S)β → 44(4p)β |
| 4.78 eV, 259.3 nm, $f = 0.0241$ | 35(d)α → 42(NO)α |
| | 39(S)α → 44(4p)α |
| 4.87 eV, 254.3 nm, $f = 0.0266$ | 34(d)α → 40(NO)α |
| | 34(d)α → 41(NO)α |
| | 38(S)β → 45(4p)β |
| 4.95 eV, 250.3 nm, $f = 0.0226$ | 39(S)α → 46(4p)α |
| | 38(S)β → 46(4p)β |
| 5.15 eV, 240.5 nm, $f = 0.0535$ | 33(d–S)α → 40(NO)α |
| | 34(d)α → 40(NO)α |
| 5.17 eV, 239.8 nm, $f = 0.0646$ | 39(S)α → 46(4p)α |



Fig. 6. Calculated electronic spectra of **I** and **II** in water.

assumption of equimolar ratio of the both isomers. In the drawings, each calculated transition is described by a Gaussian function with the height equal to the oscillator strength and the width equal to 0.09. In the description of the electronic transitions the main component of the molecular orbital is used, i.e., the bonding $\pi_{Fe–NO}$ orbital is described as 'd' if it is localised mostly on a d iron

orbital, and as $\pi^*_{NO}$ if it is localised on a $\pi^*$ orbital of a nitrosyl group.

The calculated transition 642.3 nm (Table 7) is mainly of the $S_\pi \to \pi^*_{NO}$ and $S_\pi \to d$. It may be attributed to the experimental band at about 770 nm. The transition at 575.5 nm composed of $S_\pi \to \pi^*_{NO}$ and $\pi^*_{NO} \to d$ excitations can be assigned to the experimental band at about 600 nm. There is a transition with a large oscillator strength at 513.8 nm which is formed by $S_\pi \to \pi^*_{NO}$ excitation. The transitions between 335 and 318 nm are predominantly of $\pi^*_{NO} \to d$ character. They can be attributed to the experimental band at about 390 nm. There are observed two groups of transitions with oscillator strengths larger than 0.01, the first one in between 303 and 290 nm and the second one in between 280 and 270 nm. They are mostly formed by the $\pi^*_{NO} \to d$ excitations, in some of them the $d \to \pi^*_{NO}$ character may be also noted. The transitions at wavelengths below 260 nm are of Rydberg and $d \to \pi^*_{NO}$ type. The latter ones occurs for example at 250.3 nm. The calculated spectrum (Fig. 6) is similar in shape with the experimental one [19] but all bands are hypsochromically shifted.

The electronic spectrum without solvent model was also calculated for **I**. In this case, however, the transitions to the 4p orbitals of iron appeared at longer wavelengths (about 300 nm). This can be explained by a diffuse character of the charge density in the negatively charged complex and indicates a need of using solvent model in the calculations of electronic transition in such a case.

### 4.2. II

The electronic spectrum of **II** was calculated with water. The calculated excitation energies, wavelengths, oscillator strengths and the excitations with the largest coefficients are given in Table 8 for the conformation **IIA**. The calculated spectra for the other conformations are similar and they are omitted for sake of brevity. In Fig. 6, the electronic spectrum of conformations **IIA–IIC** is depicted with the assumption of equal ratio of all the conformers.

The transition calculated at the longest wave (667.2 nm) with a very small oscillator strength is composed of excitations with $\pi^*_{NO} \to d$ and $S_\pi \to d$ character. The transition at 648.0 nm is mainly of $S_\pi \to d$ type. The calculated transitions at 627.3 and 611.5 nm with somewhat larger oscillator strengths are of mixed $\pi^*_{NO} \to d$ and $S_\pi \to d$ character. The transitions about 540 nm (546.3 and 539.1 nm) and over 400 nm (447–402 nm) are of similar character. The transitions at 390.1 and 368.8 nm with small oscillator strengths and transitions between 346.9 and 284.8 nm with large oscillator strengths are mainly of $\pi^*_{NO} \to d$ character. The transition at 248.9 nm originates from $d \to \pi^*_{NO}$ excitations.

Table 8
Calculated transition energies, wavelengths, oscillator strengths and the most important excitation for **IIA** (water)

| | |
|---|---|
| 1.85 eV, 667.2 nm, $f = 0.0015$ | 35(NO–S)β → 38(d)β |
| | 36(S)β → 38(d)β |
| 1.91 eV, 648.0 nm, $f = 0.0015$ | 40(S)α → 41(NO)α |
| | 36(S)β → 39(d)β |
| | 37(S)β → 39(d)β |
| 1.97 eV, 627.3 nm, $f = 0.0080$ | 35(NO–S)β → 38(d)β |
| | 37(S)β → 38(d)β |
| 2.02 eV, 611.5 nm, $f = 0.0069$ | 35(NO–S)β → 39(d)β |
| | 37(S)β → 38(d)β |
| 2.07 eV, 598.7 nm, $f = 0.0061$ | 40(S)α → 41(NO)α |
| | 37(S)β → 39(d)β |
| 2.19 eV, 565.8 nm, $f = 0.0025$ | 39(S)α → 41(NO)α |
| | 35(NO–S)β → 38(d)β |
| | 35(NO–S)β → 39(d)β |
| 2.26 eV, 546.3 nm, $f = 0.0063$ | 40(S)α → 42(NO)α |
| | 36(S)β → 40(d)β |
| | 37(S)β → 39(d)β |
| 2.29 eV, 539.1 nm, $f = 0.0058$ | 40(S)α → 42(NO)α |
| | 31(NO–S)β → 38(d)β |
| | 36(S)β → 39(d)β |
| 2.47 eV, 500.7 nm, $f = 0.0049$ | 39(S)α → 42(NO)α |
| | 40(S)α → 42(NO)α |
| 2.77 eV, 447.2 nm, $f = 0.0062$ | 38(S)α → 42(NO)α |
| | 37(S)β → 42(d)β |
| 2.80 eV, 442.1 nm, $f = 0.0059$ | 37(S)α → 42(NO)α |
| | 34(NO–S)β → 39(d)β |
| 2.88 eV, 429.2 nm, $f = 0.0133$ | 30(NO–S)β → 39(d)β |
| | 34(NO–S)β → 38(d)β |
| 3.17 eV, 390.1 nm, $f = 0.0051$ | 30(NO–S)β → 39(d)β |
| | 33(NO–S)β → 40(d)β |
| | 34(NO–S)β → 40(d)β |
| 3.36 eV, 368.8 nm, $f = 0.0089$ | 34(NO–S)β → 41(d)β |
| | 34(NO–S)β → 42(d)β |
| 3.57 eV, 346.9 nm, $f = 0.0109$ | 31(NO–S)β → 38(d)β |
| | 33(NO–S)β → 41(d)β |
| | 34(NO–S)β → 42(d)β |
| 3.76 eV, 329.2 nm, $f = 0.0346$ | 35(S)α → 42(NO)α |
| 3.85 eV, 321.7 nm, $f = 0.0443$ | 30(NO–S)β → 42(d)β |
| | 31(NO–S)β → 40(d)β |
| | 33(NO–S)β → 42(d)β |
| 3.93 eV, 315.1 nm, $f = 0.0419$ | 31(NO–S)β → 40(d)β |
| | 32(NO)β → 40(d)β |
| | 33(NO–S)β → 42(d)β |
| 4.19 eV, 295.8 nm, $f = 0.0706$ | 31(NO–S)β → 41(d)β |
| | 32(NO)β → 41(d)β |
| 4.30 eV, 288.1 nm, $f = 0.0371$ | 30(NO–S)β → 42(d)β |
| | 31(NO–S)β → 40(d)β |
| 4.35 eV, 284.8 nm, $f = 0.0547$ | 31(NO–S)β → 42(d)β |
| | 32(NO)β → 42(d)β |
| 4.72 eV, 262.2 nm, $f = 0.0637$ | 40(S)α → 43(4p)α |
| | 31(NO–S)β → 42(d)β |

Table 8 (*continued*)

| | |
|---|---|
| 4.78 eV, 259.3 nm, $f = 0.0688$ | $40(S)\alpha \rightarrow 43(4p)\alpha$ |
| 4.97 eV, 248.9 nm, $f = 0.0150$ | $34(d–S)\alpha \rightarrow 41(NO)\alpha$ |
| | $34(d–S)\alpha \rightarrow 42(NO)\alpha$ |
| 5.06 eV, 244.7 nm, $f = 0.0092$ | $39(S)\alpha \rightarrow 44(4p)\alpha$ |
| | $40(S)\alpha \rightarrow 44(4p)\alpha$ |
| | $37(S)\beta \rightarrow 43(4p)\beta$ |

The transitions to 4p orbitals appear starting from 260 nm.

In general the calculated electronic spectrum of **II** is similar to that of **I**, only the calculated bands at wavelengths above 300 nm are broader, whereas that about 290 nm is narrower than in **I**. On the basis of the TDDFT calculated electronic spectra of **I** and **II**, it may be concluded that all transitions are of mixed CT character. The lower energy bands are mostly of LLCT ($S_\pi \rightarrow \pi^*_{NO}$) and LMCT type ($S_\pi \rightarrow d$), some higher energy transitions are mostly LMCT (with the prevailing $d \rightarrow \pi^*_{NO}$ type). The MLCT transitions of the $d \rightarrow \pi^*_{NO}$ type occur in the calculated spectra at higher energy (below 270 nm) and are mixed with the Rydberg transitions to the 4p orbitals of iron.

The appearance of Rydberg transitions in the present calculations should be treated with caution. It is known that the conventional functionals used in DFT calculations do not have the appropriate asymptotic behaviour [25–27]. According to that, the calculated transitions of energies higher than the energy of the HOMO orbital may be poorly reproduced by the TDDFT method.

## 5. Conclusions

The results of the density functional calculations can be compared with the experimental properties only for the $[(RS)_2Fe(NO)_2]^-$ compounds. In this case not only spectral UV–Vis and EPR properties but also chemical reactivities have been studied [2,18–24]. Because of lack of the X-ray measurement for the $[(CH_3S)_2Fe(NO)_2]^-$ species, the calculated structure was compared with that of the structurally similar compound of the $[(RS)_2Fe(NO)_2]$ type [21] and quite satisfactory results were obtained (Table 2). The calculated spectrum (Fig. 6) is similar in shape with the experimental one [19] but all bands are hypsochromically shifted. The calculations revealed that all the bands are of the CT character, which changes with the increase in the transition energy from LLCT ($S_\pi \rightarrow \pi^*_{NO}$) + LMCT ($S_\pi \rightarrow d$) to LMCT ($\pi^*_{NO} \rightarrow d + S_\pi \rightarrow d$) and at last to MLCT ($d \rightarrow \pi^*_{NO}$). The electronic structure of **I** can be described as the high spin ($S = 5/2$) ferric ion antiferromagnetically coupled to the two $NO^-$ ligands with

$S = 1$, with the total spin $S = 1/2$. The calculated doublet spin state is in agreement with the experiment. The antiferromagnetic coupling explains the low spin state of this complex, which is not typical for the tetrahedral iron complexes. The description of the iron centre as Fe(III) or Fe(−I) is, however, simplistic, as the calculated spin densities point at the former, whereas the net chemical behaviour is consistent with the latter approximation.

The $[(RS)_2Fe(NO)_2]^-$ complexes are known as reactive species, which are stable in solution only in the presence of a large excess of $RS^-$ [18–24]. Otherwise, the ions form readily a di-nucleated structure via formation of two RS-bridges and release of other two $RS^-$ ligands in the reversible reaction:

$$2[(RS)_2Fe(NO)_2]^- \rightleftharpoons [Fe_2(\mu\text{-}SR)_2(NO)_4] + 2RS^- \quad (1)$$
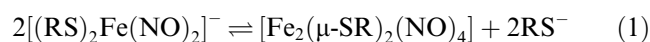
However, in the presence of a different thiol, its S-nitrosation

$$[(RS)_2Fe(NO)_2]^- + R'SH$$
$$\rightarrow R'S\text{–}NO + \text{decomposition products} \quad (2)$$
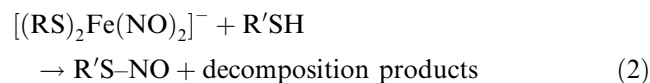
could be observed as well (where RS = L-cysteine or GSH and R′S = albumin) [2,22]. This behaviour is responsible for the role of $[(RS)_2Fe(NO)_2]^-$ in the NO-storage and NO-transport occurring in vivo [2]. The calculations presented here explian, a tendency of forming a double bound species (Eq. (1)). As the HOMO are mostly sulfur orbitals with a large space extent (Fig. 2), the effective overlap of the HOMO orbital and the LUMO orbital of the d type, between two molecules, can result in the formation of the first RS-bridge. The polarisation of the S–C bond, which becomes enhanced in the polar solvent (Table 3), a contribution of S orbitals to HOMO (Fig. 3), distorted tetrahedral geometry (Table 2) can favour the step. The next reaction steps, i.e., formation of the second RS-bridge and release of two $RS^-$ ligands may be realised in a concerted process. A considerable contribution of $\pi^*_{NO}$ to LUMO (Fig. 2) and polarisation of the NO bond enable the RS nucleophile attack followed by the Fe–No bond clevage.

Although the experimental data for the $[(RS)_3Fe(NO)]^-$ complexes are scarce, the behaviour similar to that of $[(RS)_2Fe(NO)_2]^-$ can be expected on the basis of the DFT calculations. In this complex, similarly, as in **I**, the high spin ferric ion is antiferromagnetically coupled to the $NO^-$ ligand, yielding the final quantum spin number $S = 3/2$. A slightly longer the Fe–N distance and smaller the Fe–N–O angle, than in **I**, may point at some more contribution of the Fe(III)–$NO^-$ structure, and in consequence, a slightly weaker nitrosation capacity of **II**, although it should not entail a meaningful difference in the chemical reactivity.

## Acknowledgements

## References

[1] A.R. Butler, C. Glidewell, M.H. Li, Adv. Inorg. Chem. 32 (1988) 335.

[2] P.G. Wang, M. Xian, X. Tang, X. Wu, Z. Wen, T. Cai, J.J. Janczuk, Chem. Rev. 102 (2002) 1091.

[3] J.H. Enemark, R.D. Feltham, Coord. Chem. Rev. 13 (1974) 339.

[4] R. Hoffmann, M.M.L. Chen, D.L. Thorn, Inorg. Chem. 16 (1977) 503.

[5] R. Hoffmann, M.M.L. Chen, M. Elian, M. Rossi, D.M.P. Mingos, Inorg. Chem. 13 (1974) 2666.

[6] C.A. Brown, M.A. Pavlosky, T.E. Westre, Y. Zang, B. Hedman, K.O. Hodgson, E.I. Solomon, J. Am. Chem. Soc. 117 (1995) 715.

[7] T.E. Westre, A. DiCicco, A. Filliponi, C.R. Natoli, B. Hedman, E.I. Solomon, K.O. Hodgson, J. Am. Chem. Soc. 116 (1994) 6757.

[8] C. Hauser, T. Glaser, E. Bill, T. Weyermüller, K. Wieghardt, J. Am. Chem. Soc. 122 (2000) 4352.

[9] M. Li, D. Bonnet, E. Bill, F. Neese, T. Weyermüller, K. Wieghardt, Inorg. Chem. 41 (2002) 3444.

[10] M.J. Frisch, G.W. Trucks, H.B. Schlegel, G.E. Scuseria, M.A. Robb, J.R. Cheeseman, V.G. Zakrzewski, J.A. Montgomery, Jr., R.E. Stratmann, J.C. Burant, S. Dapprich, J.M. Millam, A.D. Daniels, K.N. Kudin, M.C. Strain, O. Farkas, J. Tomasi, V. Barone, M. Cossi, R. Cammi, B. Mennucci, C. Pomelli, C. Adamo, S. Clifford, J. Ochterski, G.A. Petersson, P.Y. Ayala, Q. Cui, K. Morokuma, N. Rega, P. Salvador, J.J. Dannenberg, D.K. Malick, A.D. Rabuck, K. Raghavachari, J.B. Foresman, J. Cioslowski, J.V. Ortiz, A.G. Baboul, B.B. Stefanov, G. Liu, A. Liashenko, P. Piskorz, I. Komaromi, R. Gomperts, R.L. Martin, D.J. Fox, T. Keith, M.A. Al-Laham, C.Y. Peng, A. Nanayakkara, M. Challacombe, P.M.W. Gill, B. Johnson, W. Chen, M.W. Wong, J.L. Andres, C. Gonzalez, M. Head-Gordon, E.S. Replogle, J.A. Pople, GAUSSIAN98, Revision A.11.4, Gaussian, Inc., Pittsburgh PA, 2002.

[11] A.D. Becke, J. Chem. Phys. 98 (1993) 5648.

[12] P.J. Stevens, F.J. Devlin, C.F. Chablowski, M.J. Frisch, J. Phys. Chem. 98 (1994) 11623.

[13] M.E. Casida, in: J.M. Seminario (Ed.), Recent Developments and Applications of Modern Density Functional Theory, Theoretical and Computational Chemistry, Elsevier, Amsterdam, 1996.

[14] P.J. Hay, W.R. Wadt, J. Chem. Phys. 82 (1985) 299.

[15] T.H. Dunning Jr., P.J. Hay, in: H.F. Schaeffer (Ed.), Methods of Electronic Structure Theory, third ed., Plenum Press, New York, 1977.

[16] S. Miertus, E. Scrocco, J. Tomasi, Chem. Phys. 55 (1981) 117.

[17] M. Cossi, V. Barone, R. Cammi, J. Tomasi, Chem. Phys. Lett. 255 (1996) 327.

[18] K. Szaciłowski, J. Oszajca, A. Barbieri, A. Karocki, Z. Sojka, S. Sostero, R. Boaretto, Z. Stasicka, J. Photochem. Photobiol. A: Chem. 143 (2001) 99.

[19] S. Costanzo, S. Ménage, R. Parello, R.P. Bonomo, M. Fontecave, Inorg. Chim. Acta 318 (2001) 1.

[20] A.R. Butler, C. Glidewell, A.R. Hyde, J.C. Walton, Polyhedron 4 (1985) 797.

[21] L.M. Baltusis, K.D. Karlin, H.N. Rabinowitz, J.C. Dewan, S.J. Lippard, Inorg. Chem. 19 (1980) 2627.

[22] M. Boese, P.I. Mordvintcev, A.F. Vanin, R. Busse, A. Mulsch, J. Biol. Chem. 270 (1995) 29244.

[23] K. Szaciłowski, W. Macyk, G. Stochel, Z. Stasicka, S. Sostero, O. Traverso, Coord. Chem. Rev. 208 (2000) 277.

[24] C.L. Conrado, J.L. Bourassa, C. Egler, S. Wecskler, P.C. Ford, Inorg. Chem. 42 (2003) 2288.

[25] D.J. Tozer, N.C. Handy, J. Chem. Phys. 109 (1998) 10180.

[26] D.J. Tozer, R.D. Amos, N.C. Handy, B.O. Roos, R. Serrano-Andrés, Mol. Phys. 97 (1999) 859.

[27] M. Grüning, O.V. Gritsenko, S.J.A. van Gisbergen, E.J. Baerends, J. Chem. Phys. 114 (2001) 652.